Droplet coalescence: drainage, film rupture and neck growth in ultralow interfacial tension systems

DIRK G. A. L. AARTS† AND HENK N. W. LEKKERKERKER

Van't Hoff Laboratory, Debye Institute, Utrecht University, Padualaan 8, 3584 CH Utrecht,
The Netherlands

We study the coalescence of a drop with its bulk phase in fluid–fluid demixing colloid–polymer mixtures. Such mixtures show behaviour analogous to molecular fluid–fluid systems, but the interfacial tension is between 10^5 to 10^7 times smaller than in the molecular case. Such an ultralow interfacial tension has several important consequences and offers significant advantages in the study of droplet coalescence. The coalescence process can be divided into three consecutive stages: (i) drainage of the continuous film between droplet and bulk phase, (ii) rupture of the film, and (iii) growth of the connection. These stages can be studied within a single experiment by optical microscopy thanks to the ultralow interfacial tension in colloid–polymer mixtures, which significantly changes the relevant characteristic length and time scales. The first stage is compared with existing theories on drainage, where we show several limiting theoretical cases. The experimental drainage curves of different colloid–polymer mixtures can be scaled and then show very similar behaviour. We observe that drainage becomes very slow and eventually the breakup of the film is induced by thermal capillary waves. The time it takes for a certain height fluctuation of the interface to occur, which turns out to be an important parameter for the kinetics of the process, can be directly obtained from experiment. During the third stage we observe that the radius of the connecting neck grows linearly with time both for gas bubbles and liquid droplets with an order of magnitude that is in good agreement with the capillary velocity. Finally, partially bleaching the fluorescent dye inside the liquid droplet reveals how the surface energy is transformed into kinetic energy upon coalescence. This opens the way for a more complete understanding of the hydrodynamics involved.

1. Introduction

The process of droplet coalescence is frequently observed in everyday life. Whenever two miscible liquid drops or a liquid drop and its liquid bulk come into contact they may coalesce. The coalescence reduces the total interface area and is driven by the interfacial tension. The phenomenon has been studied since the 19th century, starting with Thomson & Newall (1885), and it is a classical example of a free-surface problem in fluid dynamics. It has important consequences, e.g. the droplet size distribution in rain is (among other processes) determined by the coalescence probability (see for

† Present address: Physical and Theoretical Chemistry Laboratory, South Parks Road, OX1 3QZ Oxford, UK.
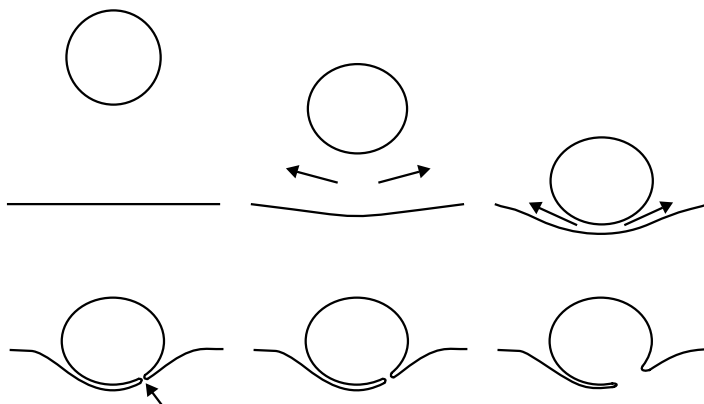
FIGURE 1. Schematic drawing of the consecutive stages – film drainage, film rupture, and neck growth – of droplet coalescence from left to right, top to bottom. Shown is the drainage of the continuous phase (i) (top row), the first connection is made (ii) and the radius of the neck grows in time (iii) (bottom row).

example Brandes, Zhang & Vivekanadan 2004). It is of practical importance as well; in many industrial applications – such as printing and sintering processes – coalescence plays a crucial role (to be either avoided or induced), see for example Frohn & Roth (2000). Recent developments in the field of microfluidics (see for example reviews by Stone, Stroock & Ajdari 2004; Squires & Quake 2005; Haeberlea & Zengerle 2007), in which fluids are manipulated on a microscopic level and miniature chemical reactions can be carried out on a chip, provide a further need to study this phenomenon.

Here, we focus on the three consecutive stages in droplet coalescence: (i) film drainage of the continuous phase between the droplet and the free interface, (ii) rupture of the film, i.e. the formation of the first connection between drop and bulk, and (iii) extrusion of the droplet material into its bulk phase, see figure 1 for a schematic of these steps. The first stage (i) has been studied for quite some time, for example Brown & Hanson (1967), Hartland (1969a,b,c), and Hartland, Yang & Jeelani (1993), although it still poses some theoretical difficulties (Jones & Wilson 1978). In many studies the drainage is followed close to the point of film rupture (ii), and step (ii) is studied in relation with step (i) (Jeffreys & Hawksley 1962; Brown & Hanson 1967); furthermore, the role of van der Waals forces has been investigated (Vrij 1966; Chen et al. 2004). Recently, significant theoretical (Eggers, Lister & Stone 1999) and numerical (Duchemin, Eggers & Josserand 2003) progress has been made in the description of the neck growth, step (iii), and in understanding the singularity that occurs during coalescence. Recently, the initial viscous coalescence has been observed experimentally (Yao et al. 2005; Thoroddsen, Takehara & Etoh (2005); Aarts et al. 2005b) and in dissipative particle dynamics simulations (Iancu 2005), as well as the inertial coalescence (Mechaca-Rocha et al. 2001; Wu, Cubaud & Ho 2004), which follows the viscous coalescence.

We make use of the properties of colloid–polymer mixtures to follow the details of coalescence in time with microscopy. Phase-separated colloid–polymer mixtures are well known to display behaviour analogous to molecular fluid–fluid systems. In addition, such mixtures are also used in industry, for example in the food industry (Dickinson & Walstra 1993). The origin of the phase separation in colloid–polymer mixtures lies in the entropy-driven attraction between the colloids, which is mediated by the polymers (Asakura & Oosawa 1954; Vrij 1976). The coexisting phases are a phase rich in colloids and poor in polymer and a phase poor in colloid and rich in

polymer. We will refer to these phases as being colloidal liquid and colloidal gas, or simply liquid and gas phases respectively. After preparing a sample in the two-phase region individual droplets of either the liquid or the gas coalesce with their bulk phase at the final stages of phase separation (Aarts, Dullens & Lekkerkerker 2005*a*). This allows us to study this process.

The main advantage of using colloid–polymer mixtures over molecular fluids has its origin in the ultralow interfacial tension of demixed colloid–polymer mixtures. Following Rowlinson & Widom (1982) and De Gennes (1979) we find that the typical magnitude of the interfacial tension γ is proportional to

$$\gamma \sim \frac{k_B T}{d^2} \tag{1.1}$$

with $k_B T$ the thermal energy and d the typical length scale at the interface, similar to the particle diameter σ_c far away from the critical point. This order of magnitude has been confirmed in experiments by Vliegenthart & Lekkerkerker (1997), de Hoog & Lekkerkerker (1999), Chen, Payandeh & Robert (2000), de Hoog & Lekkerkerker (2001) and Aarts, van der Wiel & Lekkerkerker (2003), theoretically by Vrij (1997), Brader & Evans (2000), Brader *et al.* (2002), Moncho-Jorda, Rotenberg & Louis (2003) and Aarts *et al.* (2004*a*) and recently in computer simulations by Vink & Horbach (2004*a,b*).

This ultralow interfacial tension has several important consequences. First, the equilibrium thermal roughness of the interface $L_T = \sqrt{k_B T/\gamma}$ (Mandelstam 1913; Buff, Lovett & Stillinger 1965), which is due to the thermally excited capillary waves, can become of the order of (sub)microns. Furthermore, in our systems these waves are overdamped with a characteristic decay time of the order of (tens of) seconds (Jeng *et al.* 1998). Therefore, the thermal capillary waves can be directly observed with optical microscopy, for which we found good agreement with the standard capillary wave model (Aarts, Schmidt & Lekkerkerker 2004*b*), and it is thus possible to study step (ii), the rupture of the film, on the scale of thermal capillary fluctuations. Furthermore, from the Reynolds number $Re = \rho u L/\eta$ with ρ the mass density, u the velocity, L the characteristic length and η the viscosity, we can estimate at what length inertia becomes as important as viscous dissipation. At small length and time scales the velocity u of interface motion is always proportional to $u \sim \gamma/\eta$ (Probstein 2003). At $Re = 1$ inertial terms are expected to become important, i.e. at lengths

$$L_\eta = \frac{\eta^2}{\rho\gamma}, \tag{1.2}$$

and times

$$t_\eta = \frac{L}{u} = \frac{\eta^3}{\rho\gamma^2}. \tag{1.3}$$

For ordinary water with $\gamma = 73 \, \text{mN m}^{-1}$, $\eta = 1 \, \text{mPa s}$, and $\rho = 1 \, \text{g ml}^{-1}$, inertial terms come into play at $L_\eta = 10^{-8} \, \text{m}$, which is reached in $t_\eta = 2 \times 10^{-10} \, \text{s}$, an intractably short time and length. Thus, the initial viscous regime of step (iii) is hard to observe in the laboratory for ordinary molecular liquids. To tackle this problem it is in principle possible to follow two routes: either increase the viscosity or decrease the interfacial tension. Here, we follow the latter option and decrease the interfacial tension between a factor 10^5 and 10^8 compared to the interfacial tension of water. In addition, this allows us to explore the role thermal fluctuations play in the process of droplet coalescence.

We show results for several colloid–polymer mixtures: one mixture of silica colloids and poly(dimethylsiloxane) polymer in cyclohexane, and two different mixtures of poly-(methylmetacrylate) colloids (PMMA) and poly(styrene) polymer in decalin, described in detail in §2, where also the statepoints are indicated. These yield similar results, which points to generic behaviour. The consecutive steps are described in §3 for step (i), §4 for step (ii) and §5 for step (iii). Conclusions are drawn in §6.

2. Experimental system and technique

Three different mixed colloid–polymer dispersions have been used. The first system was originally prepared by Verhaegh *et al.* (1996). The colloids are commercially available ludox spheres (Ludox AS 40 % Dupont) coated with stearyl alcohol (1-octadecanol, Merck, zur synthesis) providing steric stabilization following the method by Helden, Jansen & Vrij (1980). The particles were dispersed in cyclohexane. The (dynamic light scattering) radius R_c of the particle was 13 nm with a polydispersity of 19 % and the density was 1.60 g ml^{-1} as determined by de Hoog & Lekkerkerker (1999) and de Hoog (2001). The molecular weight M_w of the poly(dimethylsiloxane) polymers (abbreviated as PDMS, supplier: Janssen) was 91.7 kg mol^{-1} ($M_w/M_n = 1.9$, with M_n the number average molecular weight) and the density was 0.976 g ml^{-1}. The polymer's radius of gyration in cyclohexane was determined as 14 nm (de Hoog & Lekkerkerker 1999; de Hoog 2001). We will refer throughout this paper to this system as system 1 with characteristics SPC13, i.e. Silica Poly(dimethylsiloxane) in Cyclohexane with the radius of the colloid equal to 13 nm.

In addition to the system above, two fluorescent poly(methylmethacrylate) PMMA-colloids + poly(styrene) polymer dispersions were used. In the preparation of PMMA we followed the method of Bosma *et al.* (2002) slightly modified by using decalin (Merck, for synthesis) as solvent. The particles are stabilized by poly(12-hydroxy stearic acid). The fluorescent dye, 4-methylamino-ethylmethacrylate-7-nitrobenzo-2-oxa-1,3-diazol, is covalently linked to the methylmethacrylate monomers and is therefore incorporated in the particle. The (dynamic light scattering) radius R_c was 25 nm and the polydispersity was less than 10 %, estimated from scanning electron microscopy images. The particles were dispersed in decalin. As polymer, commercially available poly(styrene) (PS, Fluka) was used with a molecular weight of $M_w = 233$ kg mol^{-1} ($M_w/M_n = 1.06$) and a radius of gyration R_g in decalin of $\sim$14 nm as estimated from data in the literature (Berry 1966; Vincent 1990).

The second PMMA dispersion consisted of larger PMMA colloids labelled with the same dye and higher molecular weight polymer. The (static light scattering) radius R_c of the colloids in decalin was 71 nm and the polydispersity was around 10 %. As polymer, polystyrene (Fluka) with a molecular weigth of $M_w = 2000$ kg mol^{-1} ($M_w/M_n < 1.2$) has been used; its radius of gyration in decalin is estimated to be 43 nm from data in the literature (Berry 1966; Vincent 1990).

Throughout this paper we will refer to the first PMMA-PS dispersion as system 2 with characteristics PPD25, i.e. PMMA Poly(styrene) in Decalin with the radius of the colloid equal to 25 nm. The second PMMA-PS dispersion is referred to as system 3 or PPD71, i.e. PMMA Poly(styrene) in Decalin with the radius of the colloid equal to 71 nm. A summary of the physical properties of these systems can be found in the Appendix. Throughout the text we refer to several different statepoints the characteristics of which can also be found in the Appendix. The crucial point is that given (1.1) the interfacial tension strongly decreases going from system 1 to system 3 such that a wide range of ultralow interfacial tensions can be explored.

Samples were prepared in several types of optical cuvettes by mixing colloid- and polymer-stock dispersions and diluting with the dispersing solvent. Since all densities are known, mass fractions can be directly converted to volume fractions. For colloids we use

$$\phi_c = \frac{4}{3}\pi R_c^3 n_c$$

with n_c the number density of colloids. For polymers it is customary to use the coil volume and with the molecular weight of the polymers we obtain

$$\phi_p = \frac{4}{3}\pi R_g^3 n_p = \frac{4}{3}\pi R_g^3 \frac{m_p}{M_W} N_a,$$

where n_p is the number density of polymers, m_p the mass of polymers per total volume and N_a Avogadro's number. Now, $\phi_p = 1$ corresponds to the so-called overlap concentration. After preparing a colloid–polymer mixture, the system is homogenized either by hand or with a vortex, which is a reproducible way of homogenizing the mixture; the reproducibility has for example been checked by measuring the demixing kinetics several times after homogenization. Phase separation typically takes between 15 min and a couple of hours depending on the precise statepoint.

To study the colloid–polymer mixtures we used a transmission light microscope (Nikon Eclipse E400), placed horizontally such that in each image gravity points downwards. The setup allows monitoring using transmission light microscopy as well as laser scanning confocal microscopy (LSCM). In the transmission mode a CCD camera can be attached, which has a maximal capturing rate of 50 frames per second. In the LSCM mode a confocal scanning laser head (Nikon C1) was mounted on the microscope with a maximal capturing rate of about 1 full frame per second. Although slower in capturing, the confocal microscope has the advantage that the contrast is considerably increased. The resolution of light microscopy is of the order of the wavelength of light. For the lower magnifications this results in roughly 1 µm, whereas the confocal microscope with the highest magnification has an optical in-plane resolution of ~ 0.2 µm; the depth of focus in this case lies around 0.5 µm (Webb 1996). This means that most quantities have an uncertainty of the order of 1 µm, although in case of the thermal waves, where an oil immersion objective with a high numerical aperture was used, we have located the interface with subpixel accuracy (Aarts *et al.* 2004*b*), i.e. below 0.2 µm. Furthermore, by changing the focus the apparent size of the drop changes and the largest size corresponds to the midplane of the drop. In addition, using the transmission light microscopy mode the midplane of the drop is also defined by the sharp change in contrast.

Finally, note that the systems used are chemically carefully tailored and it is difficult to prepare them in large quantities (say more than a few ml). In addition, they are dispersed in volatile liquids making traditional methods of determining densities and viscosities more cumbersome or practically impossible. A little evaporation, for example, changes the statepoint or makes a sample in the gas phase demixing. In some cases, several techiques have been used to determine the interfacial tension; for example, for system 2 PPD25, the interfacial tension has been determined by measuring the density difference and then the capillary length in several ways: by analysing the shape of a drop resting at the interface as will be explained later (see equation (3.5)) and the shape of the interfacial profile close to a wall (Aarts 2005). From these methods the interfacial tension is found to be 0.16 µN m^{-1}. Furthermore, for this system the viscosities of liquid and gas phases were measured with an Anton Paar Physica MCR300 rheometer and we found $\eta_L = 31$ mPa s and $\eta_G = 8$ mPa s, see also the Appendix.
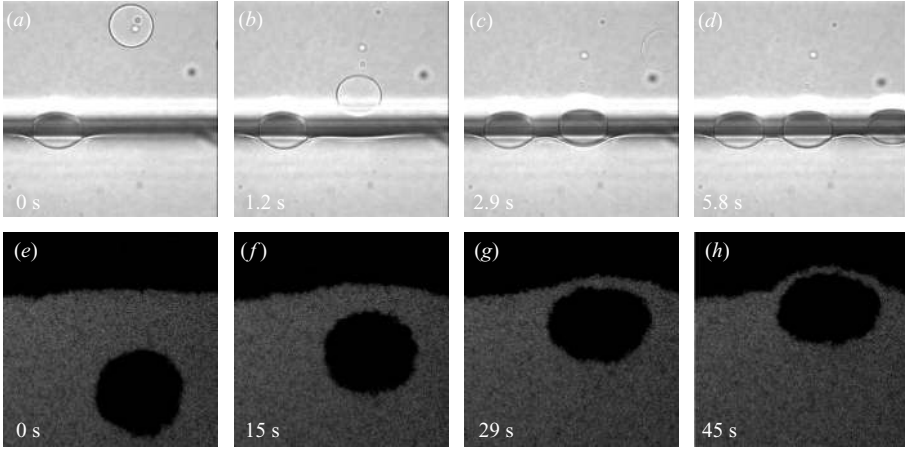
FIGURE 2. Step (i) in droplet coalescence in system 1 SPC13 as observed with transmission light microscopy (*a–d*) and system 3 PPD71 statepoint III as observed with laser scanning confocal microscopy (LSCM) (*e–h*). (*a–d*) The image size is $264 \times 264 \, \mu m^2$ and $R_d = 26 \, \mu m$. As time proceeds the shape of the drop as well as the bottom interface become distorted (*b*). The thin film drains very slowly (*c, d*) and after about 14.5 s from panel (*a*) the drop coalesces. (*e–h*) The image size is $48 \times 48 \, \mu m^2$ and $R_d = 10 \, \mu m$. The gas bubble displays similar behaviour to the liquid drop.

3. Film drainage

In the first stage of droplet coalescence the drop approaches the bulk phase, see figure 2. Here, we show results for system 1 SPC13 (top row; silica colloids and poly(dimethyl-siloxane) polymer in cyclohexane), and for system 3 PPD71 (bottom row; large PMMA colloids and poly(styrene) polymer in decalin). Initially, both the drop and the interface of the bulk phase (this interface is hereafter referred to as the surface) are undistorted, figure 2(*a, e*). In the vicinity of the surface, however, the droplet slows down and both the drop and the surface are distorted, see figure 2(*b, f*), which happens at relatively large distance as in the numerical investigations by Chi & Leal (1989). At longer times (figures 2*c, d* and 2*g, h*) the deformations become more pronounced and the film drains very slowly until it ruptures.

Far away from the bulk phase a droplet of radius R_d sediments or rises at constant velocity u_s. It will not be deformed if the capillary number Ca

$$Ca = \frac{\eta u_s}{\gamma}, \tag{3.1}$$

remains smaller than unity (Stone 1994). The sedimentation velocity u_s is proportional to $g \Delta \rho R_d^2 / \eta$ and we thus obtain from the capillary number the Bond number Bo (Stone 1994)

$$Bo = \frac{g \Delta \rho R_d^2}{\gamma}, \tag{3.2}$$

with g acceleration due to gravity and $\Delta \rho$ the buoyancy. Thus, we do not expect deformations if $Bo < 1$, i.e. $R_d < L_c \equiv \sqrt{\gamma / g \Delta \rho}$, the capillary length. The capillary length is of the order of 10–30 μm for colloid–polymer mixtures instead of 1–3 mm for molecular fluids. In experiment most droplets remain spherical while sedimenting†,

† We here use 'sedimenting' as a general term, which also applies for rising gas bubbles.

even drops with R_d slightly larger than L_c (figure 2a, e). A more precise treatment of the sedimentation velocity of a viscous sphere surrounded by a viscous medium leads to (see e.g. Lamb 1932)

$$u_s = \frac{2}{3} \frac{g \Delta \rho R_d^2}{\eta_o} \frac{\eta_o + \eta_i}{2\eta_o + 3\eta_i}. \qquad (3.3)$$

Here, η_o is the viscosity outside the drop and η_i is the viscosity inside the drop. If $\eta_i \gg \eta_o$ the well-known Stokes friction for a hard sphere is obtained: $f = F/u_s = 6\pi\eta_o R_d$ with F the force acting on the sphere. If $\eta_i = 0$ we obtain the friction for an air bubble: $f = 4\pi\eta_o R_d$.

For a solid sphere approaching a solid or free non-deformable surface exact treatments are given in Happel & Brenner (1986), which describe both the undistorted fall of (3.3) and the velocity close to the surface. The friction factor can be written as $f = 6\pi\eta_o R_d \lambda$ with $\lambda(h/R)$ the correction to the Stokes friction. When $h/R_d \ll 1$, where h is the minimal distance between sphere and surface, it becomes

$$\lambda = \frac{R_d}{h} \quad \text{and} \quad \lambda = \frac{1}{4}\frac{R_d}{h} \qquad (3.4a, b)$$

for a solid surface and for a planar free surface, respectively. These limiting equations can also be found from lubrication equations, see Reynolds (1886) and Charles & Mason (1960). Note that the factor 4 difference between a solid and a fluid interface is often observed in these types of problems. For a solid sphere approaching a deformable surface Hartland (1968) has derived expressions from lubrication theory valid for small sphere–surface separations. He finds that $h \propto t^{-1/2}$. These results were later confirmed by Jones & Wilson (1978).

However, in the experiment both the fluid drop and the fluid interface become distorted at a certain separation (figure 2), which is approximately the drop diameter. Furthermore, fluid circulates in the drop since it has a finite viscosity, which tends to speed up drainage compared to a solid sphere, and there is some constriction in the film thickness at its periphery, which slows down drainage. These last two effects are treated by Jones & Wilson (1978), who point out that these effects are not captured in simple lubrication theories. They predict several asymptotic regimes, which have been confirmed by Yiantsios & Davis (1990) using extended lubrication theories. However, the recent work of Nemer *et al.* (2004, 2007) shows the importance of subtleties overlooked in the earlier work. No full analytical treatment can be obtained and the main problem in comparison with the present experimental data is that the asymptotic limits become valid only for very small separations (Yiantsios & Davis 1990).

In figure 3 we show the minimal drop–surface separation h as a function of time t. The time $t = 0$ is defined at $h = 2R_d$, i.e. $t(h = 2R_d) = 0$. The event for a liquid drop in system 1 SPC13 is plotted in figure 3(a), which corresponds to figure 2(a–d). The top curve (plusses) is the minimal distance between drop and surface, the middle curve (open circles) is the distance between drop and (initially) undisturbed surface and the bottom curve (open squares) is the position of the surface with respect to its undisturbed position, see the inset of figure 3(a). In figure 3(b) a similar event is plotted, but in this case for a gas bubble (open symbols and plusses) and for a liquid drop (filled circles) in system 2 PPD25 (small PMMA colloids and poly(styrene) polymer in decalin). The difference in time scales between (a) and (b) is considerable and stems mainly from the difference in gas–liquid density contrast, which is much larger in system 1 SPC13, figure 3(a). In (b) the difference between gas bubbles and liquid droplets is a result of the difference in viscosity, where the liquid viscosity η_L is
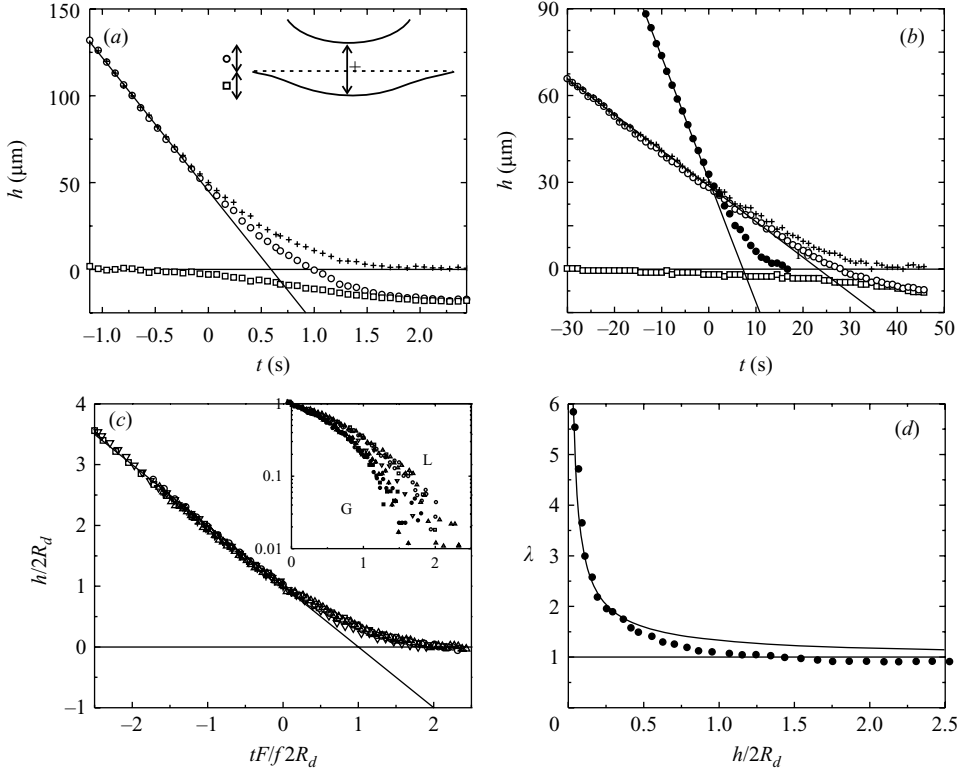
FIGURE 3. (*a*, *b*) Interface positions as a function of time for drops in (*a*) system 1 SPC13 and (*b*) 2 PPD25 (see the Appendix). (*a*) The event for a liquid drop with $R_d = 26\,\mu$m. The inset explains what the symbols denote, see also the text. (*b*) The event for a gas drop with $R_d = 15\,\mu$m (symbols as in (*a*)) and for a liquid drop with $R_d = 16\,\mu$m (for clarity, only filled circles corresponding to the circles in (*a*)). (*c*) Minimal separation for liquid drops as defined in the inset of (*a*) in terms of $2R_d$ as a function of reduced time. Data of systems 1, 2 and 3 follow a very similar curve (six different data sets are shown). The inset shows an enlargement for $t > 0$ on a log-plot. Results are added for gas bubbles (G) (three different data sets). These generally lie below the liquid drop curves (L). (*d*) The correction to the Stokes friction factor as a function of $h/2R_d$. At distances $h < 2R_d$ the friction increases rapidly. The solid curve comes from theory for a solid sphere sedimenting on a free non-deformable surface (Happel & Brenner 1986), which reaches the asymptotic value of (3.4*b*). The solid curves in (*a*–*c*) are linear fits to the first data points.

larger than the gas viscosity η_G. However, the shapes of the curves are very similar. In all cases the displacement is initially linear with time. For the events plotted in (*b*) the viscosities and density difference have been measured precisely, see the Appendix, and the initial linear velocities of the rising gas bubble and falling liquid droplet are in good agreement with equation (3.3). For example, we find for the liquid drop 4.3 μm s^{-1} from experiment and 4.2 μm s^{-1} from (3.3); for the gas bubble this is 1.2 μm s^{-1} and 1.1 μm s^{-1}.

In figure 3(*c*) several data sets for liquid drops are rescaled by plotting $h/2R_d$ vs. $t \times F/f2R_d$, with f following from (3.3), an approach similar to the one followed by Mohamed-Kassim & Longmire (2003). Thus, the initial slopes are scaled by taking the density difference as well as the inner and outer viscosity into account. We then clearly observe that data from systems 1, 2, and 3, for statepoints with different interfacial tensions and for different drop diameters ranging from 13 to

52 µm follow a very similar curve. The difference in the surface tension is easily one order of magnitude, which makes the agreement between the data for $t > 0$ somewhat remarkable, since the distortions are considerable and surface tension is expected to play a role here as well through the Bond number (Jones & Wilson 1978). This scaling implies that the problem strongly depends on $h/2R_d$, the fluid viscosities and the density difference. An enlargement of the data shows, however, that there is sufficient experimental scatter in the data to make it hard to say if there is a systematic variation as a function of viscosity contrast. The inset also shows data for rising gas bubbles, which follow a similar curve, albeit the drainage is faster in this dimensionless plot. This is in line with numerical investigations by Chi & Leal (1989). They predict a restriction at the periphery when the viscosity contrast is larger than 1 as opposed to the situation with a contrast smaller than 1, as had previously been observed in extensive experiments (Hartland 1967, 1969c). Although the general shapes of the drops seem to be governed by the Laplace pressure (see also the discussion below), the difference in viscosity contrast leads to subtle but important differences in the film profiles during drainage. Note that the system does not display any rebounding, i.e. no oscillation in the interface positions is observed. This rebounding is observed in systems where inertia cannot be neglected as in the work by Mohamed-Kassim & Longmire (2003) on impacting droplets.

In figure 3(d) we plot the Stokes' correction λ as a function of $h/2R_d$. The data are obtained by averaging and then differentiating the curves for liquid drops of system 2 PPD25. Here, we took the minimal drop–surface separation curves corresponding to the plusses in the inset of figure 3(a). Far away from the surface λ is a constant with value 0.93 in agreement with (3.3), just below the Stokes value of 1 for a hard freely sedimenting sphere. Considerable differences start occurring for $h/2R_d = 1$ and below. For such times $t > 0$ the friction increases due to solvent backflow, i.e. flow from the gap between the drop and the interface to the bulk, and drop and surface deform. The increase in friction is in reasonable agreement (within 20 %) with predictions by Happel & Brenner (1986) for a solid sphere approaching a non-deformable free surface. This is somewhat remarkable since the problem tackled in Happel & Brenner (1986) is a related but different one. It appears as if the vicinity of the interface induces rigid-like behaviour. Although many approximate and asymptotic solutions have been given in the literature (see for example Stone 1994 and references therein), it is difficult to use these on our data since it is unclear when exactly the solutions may be applied. One possibility of gaining further insight into the drainage problem is to compare these data with the approach of a solid hard sphere towards exactly the same surface. This approach is followed in de Villeneuve, Aarts & Lekkerkerker (2006), where it is observed that at small separations the same correction to Stokes' law is obtained, thus reducing the complexity of the problem.

At very small h the velocities become very low. Here, the shape of the drop depends on the interfacial tension and the density difference alone (Hartland 1969a; Princen & Mason 1965). This exterior problem can be solved within a quasi-static treatment and the shape (figure 4) is set by

$$\frac{\gamma}{g\Delta\rho} \equiv L_c^2 = \frac{l-z}{2(2/a - 1/b)}. \tag{3.5}$$

Here, $1/b$ and $1/a$ are the curvatures at and opposite to the apex. This relation can be derived by considering the pressure balance, $P_A = P_B$ and $P_C = P_D$, since points in
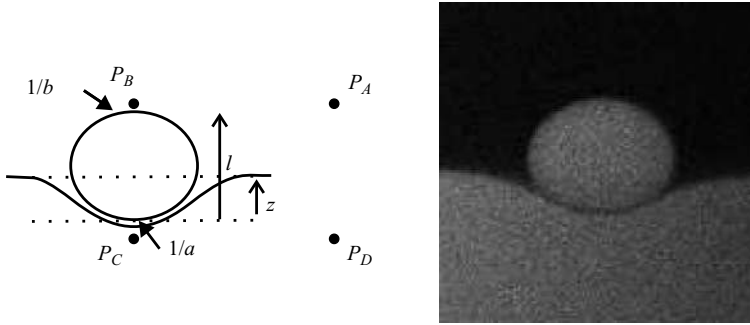
F<small>IGURE</small> 4. Explanation of the notation used in the derivation of (3.5) and an example of a liquid drop with $R_d = 19\,\mu m$, $a = 28\,\mu m$, $b = 24\,\mu m$ and $l - z = 20\,\mu m$ (system 2 PPD25) from which the capillary length can be obtained.

the same phase at the same height are in mechanical equilibrium. We find that

$$P_B = P_C - \rho_L l g + \frac{4\gamma}{a} - \frac{2\gamma}{b}, \tag{3.6}$$

and

$$P_A = P_D - \rho_L z g - \rho_G (l - z) g, \tag{3.7}$$

from which (3.5) readily follows. From these simple geometric quantities the capillary length can be obtained. For example, from the shape of the droplet shown in figure 4 (system 2) the capillary length is $18\,\mu m$ to be compared with $17.6\,\mu m$ found by analysing the interfacial profile close to a vertical hard wall (Aarts & Lekkerkerker 2004; Aarts 2005).

4. Film breakup

The role of thermally excited capillary waves (Mandelstam 1913; Buff *et al.* 1965) in the second stage of droplet coalescence has long been a topic of speculation, first started by Vrij (1966) and Scheludko (1967). The mechanism of the breakup of the film between drop and bulk phase (step (ii)) is elusive in molecular fluids; here it is evident that thermal capillary waves induce the spontaneous breakup, which occurs when two opposite bulges at the two interfaces meet (not necessarily symmetrically), see figure 5. This equilibrium surface roughness can be directly observed by microscopy due to the ultralow interfacial tension, which gives rise to a large thermal length L_T. For clarity figure 5 also displays the typical images we obtain for the free interface, i.e. without an approaching or coalescing droplet. The probability for two bulges meeting depends on the interface roughness and on the interface correlation length and time. The question is what time does it take for a height fluctuation $h \geqslant h^*$ to occur on a certain surface area. Heights are with respect to the mean interface height.

From experiment it is possible to obtain the waiting times at a free interface as a function of the observed length L, where we have followed ideas from von Smoluchowski (1916) and Becker (1966). After locating the interface position (Aarts *et al.* 2004*b*), which for example can be done by writing the total intensity along one column as the sum of the intensity of the liquid phase times the height of the liquid phase and the intensity of the gas phase times the height of the gas phase, or by fitting a tangent hyperbolic function through the intensity along a single column, which leads to very similar results, we construct a space–time plot in the following
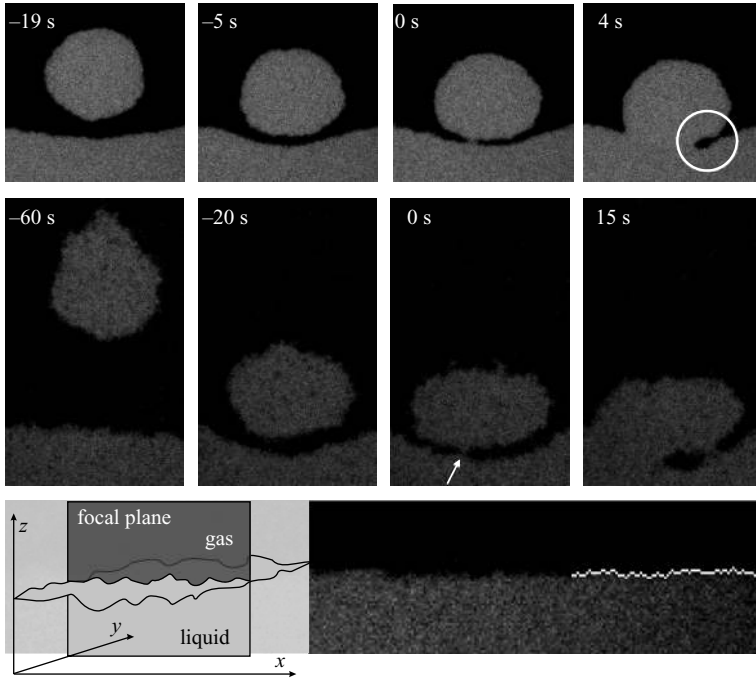
FIGURE 5. Coalescence of colloidal liquid droplets with the bulk liquid phase in system 3 PPD71. Top row, coalescence of a droplet of diameter 16.5 µm for statepoint I (far away from the critical point); middle row, coalescence of a droplet of diameter 21.8 µm for statepoint IV (close to the critical point). The three consecutive steps of the coalescence event can be followed in time (as indicated, where $t = 0$ now corresponds to the instant of film breakup). Clearly, the capillary waves at both interfaces induce the breakup of the confined gas layer. The white circle marks the typical shape as predicted by Eggers *et al.* (1999). In the series in the middle row, the arrow denotes the place of film breakup. In this case, a second connection is made and the gas phase is being trapped in the liquid phase. The bottom row shows a typical image ($17.5 \times 85 \, \mu m^2$; statepoint II) obtained for the free interface. The focal (viewing) plane is perpendicular to the interface (see inset). The bright spots at the right indicate the surface location.

manner: if $h(x, t) > h^*$ the value is 1 (white), otherwise it remains 0 (black), see figure 6(*a*) for an example of statepoint II of system 3 PPD71 with $h^* = 0.41 \, \mu m$. Next, we divide the system along x in a number of patches with length L. If at any point in this patch a white pixel is found the complete patch turns white, which means that at that time in that patch a fluctuation of at least the predefined height has occurred. This leads to images as in figure 6(*b*), which is for the same statepoint as in (*a*), but now with $h^* = 0.82 \, \mu m$. In this case we took $L = 17.5 \, \mu m$. We now identify the waiting time $\theta(h^*)$ as the average time for which the patches are 0. We can thus write

$$\theta(h^*) = \frac{M \, \Delta t}{k}, \tag{4.1}$$

where M is the total number of white patches, Δt the time between subsequent patches and k the number of jumps from 0 to 1. In constructing the waiting times it was found that these are very sensitive to noise. To cope with this we have averaged over 1000 frames. Furthermore, along the x coordinate we span 140 µm, but only the inner 105 µm is used (i.e. we left out two columns of 17.5 µm on each side), which
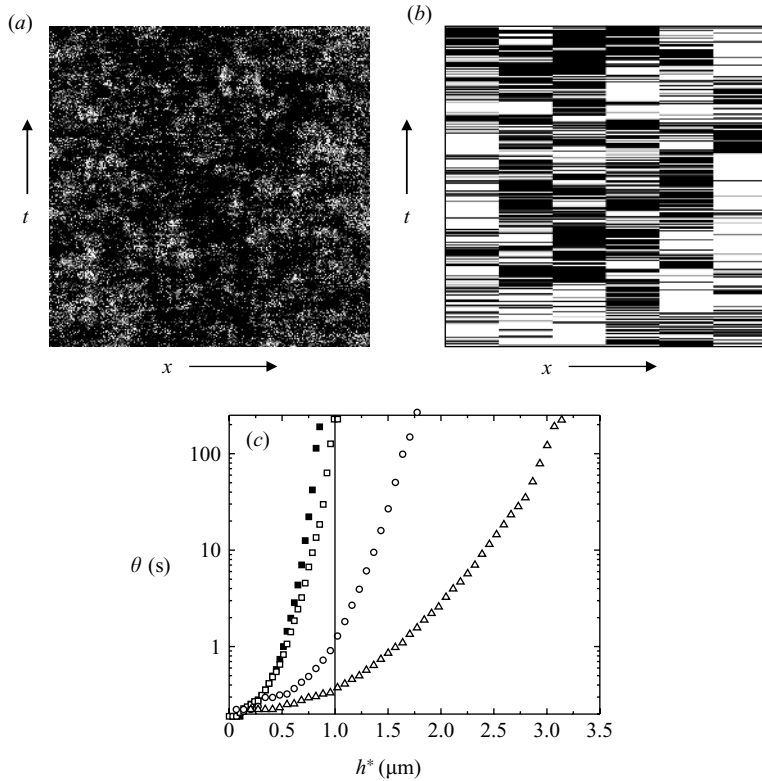
FIGURE 6. (a) Space–time plot for statepoint II, system 3 PPD71, with $h^* = 0.41\,\mu m$. x spans $140\,\mu m$ and t spans $112\,s$ (of the maximum of $223\,s$). (b) Space–time plot for the same statepoint as in (a), but for $h^* = 0.82\,\mu m$, divided into patches as explained in the text. Here, x spans $105\,\mu m$ and t spans $86\,s$. The patches have a length L of $17.5\,\mu m$. (c) Data points for $L = 17.5\,\mu m$ and for three different statepoints: I (squares), II (circles) and III (triangles) approaching the critical point. The filled squares are for a mirror event of the open squares with negative excursions and plotted against $|h^*|$. The vertical line indicates $h^* = 1\,\mu m$.

is slightly less noisy, because of the boundary effects of the microscopy objective used. In figure 6(c) we have plotted the times as a function of h^* for three different statepoints approaching the critical point, from left to right statepoints I, II, and III. Clearly, the waiting times rise steeply as a function of h^*. Analysing negative fluctuations, i.e. $h < h^*$ and $h^* < 0$, leads – given the experimental uncertainty – to a symmetric situation as shown by the filled symbols in figure 6(c), which is in line with the observation that the height distributions are symmetrical (Gaussian) distributions (Aarts et al. 2005c). Note that any inaccuracies in locating the interface position will not be of importance in the construction of correlation functions, performed in order to measure the interfacial tensions, but will show up in these single interface position properties, possibly explaining the small discrepancy between the positive and negative curves.

Following the ideas from von Smoluchowski (1916) and Becker (1966) it is possible to connect the waiting times $\theta(s)$ with the height distribution $P(h)$ through the relation

$$\theta(s) \sim \frac{\tau}{\omega(h^*)} \tag{4.2}$$

where τ is a (statepoint-dependent) characteristic time and

$$\omega(h^*) = \int_{h^*}^{\infty} P(h)\mathrm{d}h. \tag{4.3}$$

For $h^* > \sqrt{\langle h^2 \rangle}$ we can approximate the integral over the Gaussian height distribution on the right-hand side of (4.3) by

$$\omega(h^*) = \frac{\exp[-h^{*2}/2\langle h^2 \rangle]}{2\sqrt{\pi}\ h^*/\sqrt{2\langle h^2 \rangle}} \tag{4.4}$$

This expression together with (4.2) explains why the logarithm of the waiting time increases, to a good approximation, quadratically with h^*, see figure 6(c). Moreover, going from statepoint I to statepoint III we are approaching the critical point leading to a decrease in γ and an increase in $\langle h^2 \rangle$ (statepoint I: $\langle h^2 \rangle = 0.082\ \mu\mathrm{m}^2$, statepoint II: $\langle h^2 \rangle = 0.235\ \mu\mathrm{m}^2$, statepoint III: $\langle h^2 \rangle = 0.646\ \mu\mathrm{m}^2$). Since the waiting depends on the scaled variable $x = h^*/\sqrt{2\langle h^2 \rangle}$, for a given value of h^* the waiting time will be smaller for larger values of $\langle h^2 \rangle$. This is clearly seen in figure 6(c).

Based on many observations ($\sim$100) it is observed that in droplet coalescence the connection is typically made at film thicknesses of $\sim$1 μm for samples reasonably close to the critical point in system 3, i.e. when the separation reaches 1 μm coalescence occurs within 1 s. As can be seen from the waiting times in figure 6(c) such a fluctuation typically occurs in a few seconds. Since the droplet 'sees' a certain area, the connection at such thicknesses does not seem unreasonable. For samples away from the critical point the roughness is less pronounced and the film rupture occurs at smaller separations. In such instances the size of the colloids and polymers may come into play. In general we observe that below a certain droplet–surface separation, drainage becomes so slow that a spontaneous connection mediated by the capillary waves occurs faster than further drainage.

5. Neck growth

At the connection point a liquid bridge is formed and the radius of the neck increases in time, see figure 7. The opening speed of the bridge results from a competition between the capillary forces driving the coalescence, and the viscous forces slowing it down. Equating these two forces (i.e. setting the capillary number to unity in (3.1)) leads to a time dependence of the radius of the neck R_n as (Eggers *et al.* 1999)

$$R_n(t) \propto \frac{\gamma}{\eta_i} t. \tag{5.1}$$

This coalescence mechanism leads to very large speeds in ordinary molecular fluids: for water the capillary velocity is about $70\,\mathrm{m\,s}^{-1}$. The full theory predicts only logarithmic corrections to this. Eggers *et al.* (1999) find

$$R_n(t) = -\frac{\gamma}{\pi\eta_i} t\ \ln\left(\frac{\gamma}{\eta_i R_d} t\right), \tag{5.2}$$

for a viscous drop in inviscid surroundings. The shape of this solution remains the same when the viscosity of the surrounding phase is incorporated in the problem.

At longer times it is either the viscous or the inertial forces that slow down the coalescence. This depends on the relative importance of these two forces and can be found from the Reynolds number Re, as explained in §1. If inertia is dominant, i.e.
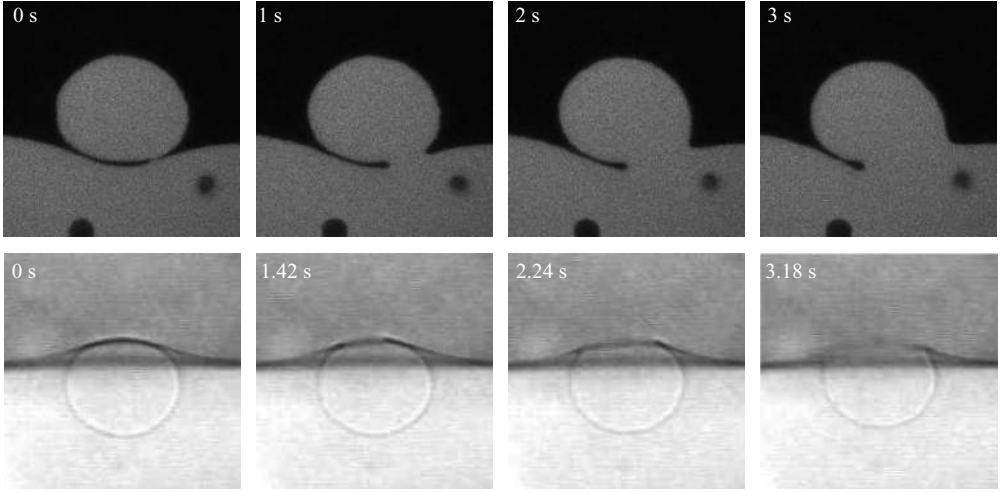
FIGURE 7. Neck growth in coalescence (system 2 PPD25) for a liquid drop with $R_d = 15\,\mu$m (top row, image size $59 \times 59\,\mu$m^2, LSCM) and a gas bubble of $R_d = 16\,\mu$m (bottom row, image size $69 \times 69\,\mu$m^2, transmission light microcsopy). The gas bubble breaks more symmetrically in comparison with the liquid drop. The typical retracting shape in the top row can again be observed (Eggers *et al.* 1999), see also figure 5.

$Re > 1$, the radius increases as (Eggers *et al.* 1999; Duchemin *et al.* 2003)

$$R_n(t) \propto \left(\frac{\gamma R}{\rho} \right)^{1/4} \sqrt{t}, \qquad (5.3)$$

where R is the radius of the undeformed drop. But in colloid–polymer mixtures this occurs at lengths L_η and times t_η, on the order of metres and hours owing to the ultra-low interfacial tension. It is therefore very unlikely that this square-root regime will be reached. On the contrary, the first regime of viscous coalescence is very hard to observe for molecular fluids, since the initial velocities are huge (70 m s^{-1}) and only by increasing the viscosity drastically and using ultrafast cameras is the initial regime observed in molecular fluids as well (Yao *et al.* 2005; Aarts *et al.* 2005*b*; Thoroddsen *et al.* 2005).

In figure 7 we show a coalescing liquid drop captured with LSCM (top row) and a coalescing gas bubble captured with transmission light microscopy (bottom row) for system 2 PPD25. Although the contrast obtained with LSCM is much better than with light microscopy the coalescence is too fast to be followed with LSCM in great detail. In principle, this could be solved by using system 3 PPD71, which has even slower dynamics, but in this system first connections are often made at several points at more or less the same time, which makes the determination of the opening speed difficult. Furthermore, in the case of multiple connections an instability may occur and a droplet of the film phase is trapped in the bulk phase, which can be verified by following the drops as a function of time, as shown here for system 1 in figure 8 (*a–d*), in line with ideas by Eggers *et al.* (1999). In addition, with LSCM it is difficult to determine if the growth is in or out of the field of focus, see also §2.

Finally, we observe that the coalescence can occur anywhere in the contacting drop bulk area. For gas droplets the first connection is often made in the top of the gas droplet, which leads to a symmetric breakup. For liquid drops the first connection is made anywhere at this area, but more often at the periphery in line with the
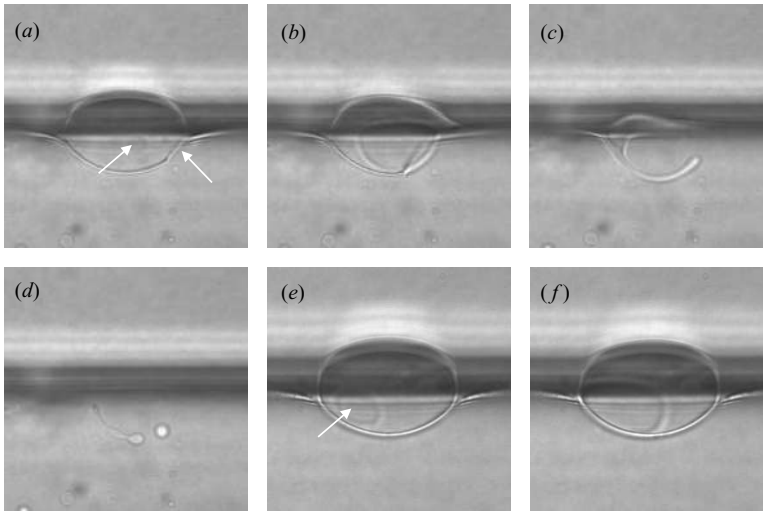
FIGURE 8. Coalescence of liquid droplets (system 1 SPC13). (*a–d*) two connections are made and gas phase is left behind. The instabilities on the gas cylinder can be clearly observed (*c, d*). The image size is $128 \times 128 \, \mu m^2$. The total time span is 2.6 s. (*e, f*) Asymmetry in growth after a first connection at the periphery of the draining film. The image size is $128 \times 128 \, \mu m^2$ and the time difference is 0.26 s. The white arrows point at connections.

predictions of Jones & Wilson (1978) about the precise shape during drainage, who show that at the periphery the drop-surface separation is minimal.

The difference between gas and liquid drops points to subtle differences in the shape of the drop and surface during drainage (step (i)). As was observed in early measurements reported by Hartland there is some constriction at the periphery when the drop viscosity is larger than the surrounding viscosity, an effect that is absent for a low-viscosity drop surrounded by a high-viscosity phase (Hartland 1967, 1969*c*). In that case, the minimal distance between drop and interface is found in the centre. These observations by Hartland were later confirmed by Chi & Leal (1989). If the first connection is not on the central symmetry axis this may lead to an asymmetric neck growth after a certain time, see figure 8(*e, f*).

Figure 9 shows the radius of the neck R_n as a function of time. The upper data correspond to coalescing gas bubbles, the lower data to coalescing liquid droplets. Clearly, a linear dependence is observed with no sign of a logarithmic correction, possibly since the logarithmic regime is expected to occur at very small times after coalescence (Eggers *et al.* 1999). The slopes of the lines are $5.7 \, \mu m \, s^{-1}$ for the gas bubbles and $2.1 \, \mu m \, s^{-1}$ for the liquid droplets. Applying the scaling relation (5.1) we expect coalescing velocities of the order of $20 \, \mu m \, s^{-1}$ for the gas bubble and $5.2 \, \mu m \, s^{-1}$ for the liquid drop without taking the viscosity of the outer fluid into account. Thus, for this statepoint we have $0.3 \gamma / \eta$ for gas bubble and $0.4 \gamma / \eta$ for liquid drop coalescence in equation (5.1). Hence, the gas bubble is slowed down more by its relatively viscous surroundings than the liquid droplet. Clearly, the observed velocities are set by the capillary velocity. However, making a quantitative prediction for the viscosity ratios such as the one in the current experiment remains a theoretical challenge.

Another point of discussion in the hydrodynamics of coalescence is where the droplet material goes and what the flow pattern is; the surface free energy gained is transformed into flow, which redistributes the material. By bleaching either the coalescing drop or the bulk phase in which the drop is coalescing, it is possible to
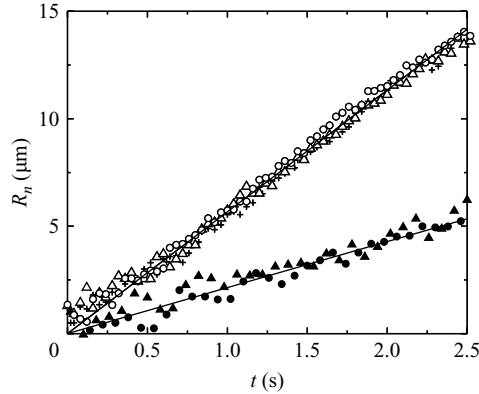
FIGURE 9. Radius of the neck R_n as a function of time for gas bubbles (open symbols; three different events with $R_d = 16$, 17 and 18 μm) and liquid droplets (closed symbols; two different events with $R_d = 15$ and 17 μm). The curves are linear fits to the data. The linear behaviour can be observed up to several times $\eta_i R_d / \gamma$, in contrast to experiments with molecular fluids (Aarts *et al.* 2005*b*). System 2 PPD25.
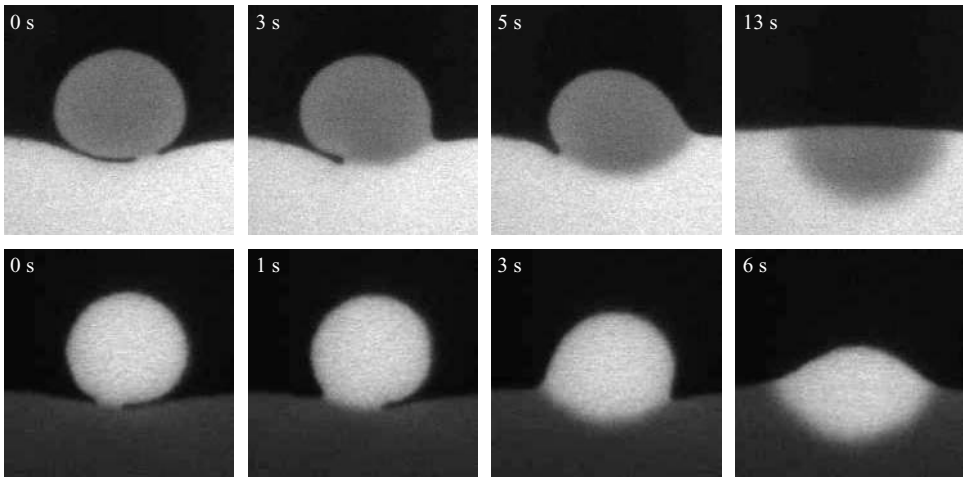

FIGURE 10. By bleaching either the droplet (top row, 56×56 μm^2) or the bulk liquid phase (bottom row, 41×41 μm^2) the coalescence event can be followed in great detail. After the connection is made, the interfacial tension acts to minimize its surface and the neck grows as a function of time. This causes the drop material to be pushed inside the bulk phase. It forms a hemisphere and the droplet material then spreads by diffusion. System 2 PPD25.

follow the liquid material into the bulk phase, see figure 10. Clearly, the interfaces first retract and in the next step the liquid material is pushed into the bulk phase. This is similar to observations on viscous fluids made by Mohamed-Kassim & Longmire (2004), where inertial terms were, however, important leading to large capillary waves at the interfaces. In our case the coalescing drop forms a clear hemisphere independent of where the first connection takes place. The liquid drop material then spreads due to diffusion which is a relatively slow process. In fact, by carefully inspecting figure 10 we observe that in the top row the crucial wave fluctuation originates from the bulk phase, while in the bottom row it originates from the droplet. Another coalescence event also provides information. In figure 11 a liquid drop coalesces on top of a gas bubble that is close to coalescence. Owing to the flow of the liquid material into
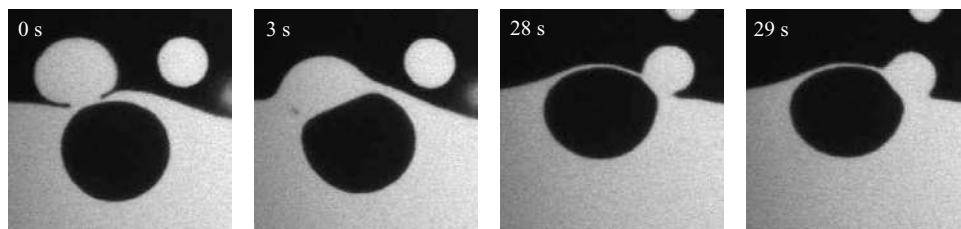
FIGURE 11. The liquid drops push their material into the thin liquid film, which distorts the interface at the gas bubble side as well. The image size is $84 \times 84\,\mu\mathrm{m}^2$. System 2 PPD25.

the thin draining liquid film we see the film being distorted up to a level where the interface becomes flat. These observations may contribute to a further understanding of the hydrodynamics of coalescence.

6. Conclusion

We have shown the three consecutive stages in droplet coalescence in fluid–fluid phase separated colloid–polymer mixtures, which are unique because of their ultralow interfacial tension. The data can be obtained in a single system with light and laser scanning confocal microscopy, and comparing results for three different colloid–polymer mixtures shows that the behaviour is rather general. In stage (i) drainage of the continuous film between droplet and bulk phase occurs. The minimal distance between droplet and surface can be rescaled for liquid as well as gas drops by taking the drop size, the gas–liquid density difference and the viscosities into account. Gas and liquid drops show distinctly different behaviour; in case of the gas drops the rescaled drainage is faster. Analysing different drops from different systems shows that the resulting scaled curves are not very different. This is somewhat remarkable, given the wide range of intermediate structures formed, ranging from a spherical drop and flat surface to a strongly deformed drop and surface. From these data the friction factor can be obtained. At large separations it is in good agreement with the modified Stokes equation for a freely sedimenting/rising fluid drop, whereas it increases considerably at small distances. There, the order of magnitude of the friction factor is in reasonable agreement with theory by Happel & Brenner (1986) for a solid sphere approaching a free non-deformable surface. At very small separations the interactions between the two fluctuating interfaces are unknown; this may give rise to a Helfrich repulsion or possibly a different kind of coupling. We have, however, no indications that this is present.

The coalescence continues via the breakup of the film (ii), which is elusive in molecular fluids. Here, it is observed that the breakup is a stochastic process dominated by the thermal capillary waves. Since at these length scales and in these organic mixtures van der Waals forces between droplet and corresponding bulk phase are minimal (Israelachvili 1992) we do not need to invoke such forces to explain the coalescence, more precisely the first connection. This is still an open debate in molecular fluids (see for example Schulze, Stöckelhuber & Wenger 2001), although experiments indicate that in molecular fluids the connection between relatively large drops (O (cm)) is brought about solely by van der Waals forces (Chen *et al.* 2004). The waiting time for a certain fluctuation to occur is crucial; it can be directly obtained from experiment. From these measurements it is very likely that a fluctuation of $\sim 1\,\mu\mathrm{m}$ at a certain area occurs within a couple of seconds in the system with the lowest interfacial tensions (system 3). We are currently incorporating these findings in a theoretical model. In fact, going from system 1 to 3 we observe that stage (ii) is

reached fastest in system 3 PPD71, where the interface roughness is more pronounced and the thin intervening film does not have to drain until very small dimensions. During the third stage (iii) we observe that the neck of the connection grows linearly with time. This is a relatively fast process with respect to drainage over a distance of for example the drop diameter. The order of magnitude of the coalescence velocity is well understood from hydrodynamic scaling arguments and it is proportional to the capillary velocity. We may conclude that the breakup itself is a stochastic process by capillary waves and that before and after the breakup, hydrodynamics is important.

Appendix. Physical properties of the model colloid–polymer mixtures

These are provided in Table 1.

System 1 SPC13

		Radius (nm)	Density (g ml^{-1})	M_w (kg mol^{-1})	Refractive index
Colloid	silica	13	1.60		1.45
Polymer	PDMS	14	0.976	91.7	
Solvent	cyclohexane		0.78		1.43

ϕ_c	ϕ_p	$\Delta\rho$ (g ml^{-1})	η_L (mPa s)	η_G (mPa s)	γ (μN m^{-1})
0.21	1.59	0.233	97.1‡	8.4‡	0.58

System 2 PPD25

		Radius (nm)	Density (g ml^{-1})	M_w (kg mol^{-1})	Refractive index
Colloid	PMMA	25	1.17		1.5
Polymer	PS	14	1.05	233	
Solvent	decalin		0.88		1.48

ϕ_c	ϕ_p	$\Delta\rho$ (g ml^{-1})	η_L (mPa s)	η_G (mPa s)	γ (μN m^{-1})
0.076	0.50	0.053	31	8	0.16

System 3 PPD71

		Radius (nm)	Density (g ml^{-1})	M_w (kg mol^{-1})	Refractive index
Colloid	PMMA	71	1.17		1.5
Polymer	PS	43	1.05	2000	
Solvent	decalin		0.88		1.48

	ϕ_c	ϕ_p	$\Delta\rho$ (g ml^{-1})	η_L (mPa s)	η_G (mPa s)	γ (μN m^{-1})
I	0.110	0.65		30	12.6	0.1
II	0.093	0.58				0.034
III	0.089	0.55				0.008
IV	0.086	0.53				0.004
V	0.150	0.70	0.096			

‡de Hoog & Lekkerkerker (1999); measured at $\phi_c = 0.24$, $\phi_p = 1.57$.

TABLE 1. Summary of the physical properties of the model colloid–polymer mixtures. For system 3 five different statepoints with different concentrations of polymer and colloid are indicated. Viscosities of the liquid and gas phases are denoted by η_L and η_G, respectively.

REFERENCES

Aarts, D. G. A. L. 2005 *J. Phys. Chem. B* **109**, 7407.

Aarts, D. G. A. L., Dullens, R. P. A. & Lekkerkerker, H. N. W. 2005*a* *New J. Phys.* **7**, 40.

Aarts, D. G. A. L., Dullens, R. P. A., Lekkerkerker, H. N. W., Bonn, D. & van Roij, R. 2004*a* *J. Chem. Phys.* **120**, 1973.

Aarts, D. G. A. L. & Lekkerkerker, H. N. W. 2004 *J. Phys.: Condens. Matter* **16**, S4231.

Aarts, D. G. A. L., Lekkerkerker, H. N. W., Guo, H., Wegdam, G. & Bonn, D. 2005*b* *Phys. Rev. Lett.* **95**, 164503.

Aarts, D. G. A. L., Schmidt, M. & Lekkerkerker, H. N. W. 2004*b* *Science* **304**, 847.

Aarts, D. G. A. L., Schmidt, M., Lekkerkerker, H. N. W. & Mecke, K. R. 2005*c* *Adv. Solid State Phys.*

Aarts, D. G. A. L., van der Wiel, J. H. & Lekkerkerker, H. N. W. 2003 *J. Phys.: Condens. Matter* **15**, S245.

Asakura, S. & Oosawa, F. 1954 *J. Chem. Phys.* **22**, 1255.

Becker, R. 1966 *Theorie der Wärme*. Springer.

Berry, G. C. 1966 *J. Chem. Phys.* **44**, 4550.

Bosma, G., Pathmamanoharan, C., de Hoog, E. H. A., Kegel, W. K., van Blaaderen, A. & Lekkerkerker, H. N. W. 2002 *J. Colloid Interface Sci.* **245**, 292.

Brader, J. M. & Evans, R. 2000 *Europhys. Lett.* **49**, 678.

Brader, J. M., Evans, R., Schmidt, M. & Löwen, H. 2002 *J. Phys.: Condens. Matter* **14**, L1.

Brandes, A.E., Zhang, G.F. & Vivekanadan, J. 2004 *J. Appl. Met.* **43**, 461.

Brown, A. H. & Hanson, C. 1967 *Nature* **214**, 76.

Buff, F. P., Lovett, R. A. & Stillinger, F. H. 1965 *Phys. Rev. Lett.* **15**, 621.

Charles, G. E. & Mason, S.G. 1960 *J. Colloid Sci.* **15**, 236.

Chen, B. H., Payandeh, B. & Robert, M. 2000 *Phys. Rev.* E **62**, 2369.

Chen, N., Kuhl, T., Tadmor, R., Lin, Q. & Israelachvili, J. N. 2004 *Phys. Rev. Lett.* **92**, 024501.

Chi, B. K. & Leal, L. G. 1989 *J. Fluid Mech.* **201**, 123.

De Gennes, P.G. 1979 *Scaling Concepts in Polymer Physics*. Cornell University Press.

Dickinson, E. & Walstra, P. 1993 *Food Colloids and Polymers: Stability and Mechanical Properties*. Cambridge: Royal Society of Chemistry.

Duchemin, L., Eggers, J. & Josserand, C. 2003 *J. Fluid Mech.* **487**, 167.

Eggers, J., Lister, J. R. & Stone, H. A. 1999 *J. Fluid Mech.* **401**, 293.

Frohn, A. & Roth, N. 2000 *Dynamics of Droplets*. Springer.

Haeberlea, S. & Zengerle, R. 2007 *Lab on a Chip* **7**, 1094.

Happel, J. & Brenner, H. 1986 *Low Reynolds Number Hydrodynamics*. Martinus Nijhoff.

Hartland, S. 1967 *Trans. Inst. Chem. Engrs* **45**, T102.

Hartland, S. 1968 *J. Colloid Interface Sci.* **26**, 383.

Hartland, S. 1969*a* *Can. J. Chem. Engng* **47**, 221.

Hartland, S. 1969*b* *Chem. Engng Sci.* **24**, 987.

Hartland, S. 1969*c* *Chem. Engng Sci.* **24**, 611.

Hartland, S., Yang, B. & Jeelani, S. A. K. 1993 *Chem. Engng Sci.* **49**, 1313.

Helden, A. K., Jansen, J. W. & Vrij, A. 1980 *J. Colloid Interface Sci.* **77**, 418.

de Hoog, E. H. A. 2001 Interfaces and crystallization in colloid-polymer suspensions. PhD thesis, Utrecht University.

de Hoog, E. H. A. & Lekkerkerker, H. N. W. 1999 *J. Phys. Chem. B* **103**, 5274.

de Hoog, E. H. A. & Lekkerkerker, H. N. W. 2001 *J. Phys. Chem. B* **105**, 11636.

Iancu, F. O. 2005 Droplet dynamics in a fluid environment. a mesoscopic simulation study. PhD thesis, Technical University Delft.

Israelachvili, J. N. 1992 *Intermolecular and Surface Forces*. Academic.

Jeffreys, G. V. & Hawksley, J. L. 1962 *J. Appl. Chem.* **12**, 329.

Jeng, U. S., Esibov, L., Crow, L. & Steyerl, A. 1998 *J. Phys.: Condens. Matter* **10**, 4955.

Jones, A. F. & Wilson, S. D. R. 1978 *J. Fluid Mech.* **87**, 263.

Lamb, H. 1932 *Hydrodynamics*. Cambridge University Press.

Mandelstam, L. 1913 *Ann. Phys.* **41**, 609–624.

MECHACA-ROCHA, A., MARTÍNEZ-DÁVALOS, A., NÚÑEZ, R., POPINET, S. & ZALESKI, S. 2001 *Phys. Rev.* E **63**, 046309.

MOHAMED-KASSIM, Z. & LONGMIRE, E. K. 2003 *Phys. Fluids* **15**, 3263.

MOHAMED-KASSIM, Z. & LONGMIRE, E. K. 2004 *Phys. Fluids* **16**, 2170.

MONCHO-JORDA, A., ROTENBERG, B. & LOUIS, A. A. 2003 *J. Chem. Phys.* **119**, 12667–12672.

NEMER, M. B., CHEN, X., PAPADOPOULOS, D. H., BLAWZDZIEWICZ, J. & LOEWENBERG, M. 2004 *Phys. Rev. Lett.* **92**, 114501.

NEMER, M. B., CHEN, X., PAPADOPOULOS, D. H., BLAWZDZIEWICZ, J. & LOEWENBERG, M. 2007 *J. Colloid Interface Sci.* **308**, 1.

PRINCEN, H. M. & MASON, S. G. 1965 *J. Colloid Sci.* **20**, 246.

PROBSTEIN, R. F. 2003 *Physicochemical Hydrodynamics,* section 10.2. John Wiley & Sons.

REYNOLDS, O. 1886 *Phil. Trans. R. Soc. Lond.* **177**, 157.

ROWLINSON, J. S. & WIDOM, B. 1982 *Molecular Theory of Capillarity*. Clarendon.

SCHELUDKO, A. 1967 *Adv. Colloid Interface Sci.* **44**, 391.

SCHULZE, H. J., STÖCKELHUBER, K. W. & WENGER, A. 2001 *Colloids Surf.* A **192**, 61.

VON SMOLUCHOWSKI, M. 1916 *Phys. Zeitschrift* **17**, 537.

SQUIRES, T. M. & QUAKE, S. R. 2005 *Rev. Mod. Phys.* **77**, 977.

STONE, H. A. 1994 *Annu. Rev. Fluid Mech.* **26**, 65.

STONE, H. A., STROOCK, A. D. & AJDARI, A. 2004 *Annu. Rev. Fluid Mech.* **36**, 381.

THOMSON, J. J. & NEWALL, H. F. 1885 *Proc. R. Soc. Lond.* **39**, 417.

THORODDSEN, S. T., TAKEHARA, K. & ETOH, T. G. 2005 *J. Fluid Mech.* **527**, 85.

VERHAEGH, N. A. M., VAN DUIJNEVELDT, J. S., DHONT, J. K. G. & LEKKERKERKER, H. N. W. 1996 *Physica* A **230**, 409.

DE VILLENEUVE, V. W. A., AARTS, D. G. A. L. & LEKKERKERKER, H. N. W. 2006 *Colloids Surf.* A **282–283**, 61.

VINCENT, B. 1990 *Colloids Surf.* **50**, 241.

VINK, R. L. C. & HORBACH, J. 2004a *J. Chem. Phys.* **121**, 3253.

VINK, R. L. C. & HORBACH, J. 2004b *J. Phys.: Condens. Matter* **16**, S3807.

VLIEGENTHART, G. A. & LEKKERKERKER, H. N. W. 1997 *Prog. Colloid Polym. Sci.* **105**, 27.

VRIJ, A. 1966 *Disc. Faraday Soc.* **42**, 23.

VRIJ, A. 1976 *Pure Appl. Chem.* **48**, 471.

VRIJ, A. 1997 *Physica* A **235**, 120.

WEBB, R. H. 1996 *Rep. Prog. Phys.* **59**, 427.

WU, M., CUBAUD, T. & HO, C. 2004 *Phys. Rev.* E **16**, L51.

YAO, W., MARIS, J. H., PENNINGTON, P. & SEIDEL, G. M. 2005 *Phys. Rev.* E **71**, 016309.

YIANTSIOS, S. G. & DAVIS, R. H. 1990 *J. Fluid Mech.* **217**, 547.